In vivo measurement of trabecular meshwork stiffness in a corticosteroid-induced ocular hypertensive mouse model

Guorong Li[a], Chanyoung Lee[b], Vibhuti Agrahari[c], Ke Wang[b], Iris Navarro[a], Joseph M. Sherwood[d], Karen Crews[e], Sina Farsiu[a,f], Pedro Gonzalez[a], Cheng-Wen Lin[e], Ashim K. Mitra[g], C. Ross Ethier[b,1], and W. Daniel Stamer[a,f,1]

[a]Department of Ophthalmology, Duke University, Durham, NC 27710; [b]Coulter Department of Biomedical Engineering, Georgia Institute of Technology/Emory University, Atlanta, GA 30332; [c]Department of Biopharmaceutical Sciences, Bernard J Dunn School of Pharmacy, Shenandoah University, Winchester, VA 22601; [d]Department of Bioengineering, Imperial College London, London SW72AZ, United Kingdom; [e]Research and Development, Aerie Pharmaceuticals, Inc., Durham, NC 27703; [f]Department of Biomedical Engineering, Duke University, Durham, NC 27710; and [g]School of Pharmacy, University of Missouri-Kansas City, Kansas City, MO 64108

Edited by Joel S. Schuman, New York University, and accepted by Editorial Board Member Jeremy Nathans December 10, 2018 (received for review August 29, 2018)

Ocular corticosteroids are commonly used clinically. Unfortunately, their administration frequently leads to ocular hypertension, i.e., elevated intraocular pressure (IOP), which, in turn, can progress to a form of glaucoma known as steroid-induced glaucoma. The pathophysiology of this condition is poorly understood yet shares similarities with the most common form of glaucoma. Using nanotechnology, we created a mouse model of corticosteroid-induced ocular hypertension. This model functionally and morphologically resembles human ocular hypertension, having titratable, robust, and sustained IOPs caused by increased resistance to aqueous humor outflow. Using this model, we then interrogated the biomechanical properties of the trabecular meshwork (TM), including the inner wall of Schlemm's canal (SC), tissues known to strongly influence IOP and to be altered in other forms of glaucoma. Specifically, using spectral domain optical coherence tomography, we observed that SC in corticosteroid-treated mice was more resistant to collapse at elevated IOPs, reflecting increased TM stiffness determined by inverse finite element modeling. Our noninvasive approach to monitoring TM stiffness in vivo is applicable to other forms of glaucoma and has significant potential to monitor TM function and thus positively affect the clinical care of glaucoma, the leading cause of irreversible blindness worldwide.

nanoparticle | glaucoma | optical coherence tomography | finite element modeling | Schlemm's canal

Due to their antiinflammatory, antiangiogenic, and antipermeability properties (1), corticosteroids are widely used in the eye clinic to treat a variety of disorders, such as macular edema, age-related macular degeneration, diabetic retinopathy, and uveitis (2–7), and, after cataract surgery, to reduce inflammation (8). Unfortunately, ocular hypertension [elevated intraocular pressure (IOP)] is the major adverse event following ocular corticosteroid treatment, occurring in a dose-dependent manner regardless of delivery route. If left untreated, ocular hypertension typically leads to irreversible glaucomatous vision loss (9).

To understand the processes that underlie corticosteroid-induced ocular hypertension, animal models have been developed in several species (10–22). Here we focus on the mouse, which has several important advantages over other nonprimate species for studying ocular hypertension. Notably, the murine conventional outflow pathway, central to controlling IOP and comprising the trabecular meshwork (TM) and Schlemm's canal (SC), is remarkably similar to the human outflow pathway in its anatomy and physiology. Further, recent data from our group using atomic force microscopy in excised eyes has shown that the TM is stiffer in corticosteroid-induced ocular hypertensive mice, similar to the increased stiffness observed in TM/inner wall of SC of human eyes with primary open-angle glaucoma (23, 24). In fact, we have shown that a significant positive correlation exists between outflow resistance and TM stiffness in both humans and mice, including in corticosteroid-treated mice (24, 25).

Several corticosteroid-induced ocular hypertension mouse models have been created using either systemic or topical routes of delivery (18, 20–22). However, each model has drawbacks, including technical demands, modest efficacy, adverse events, or limited duration. To achieve slow, sustained, and controlled release of a potent synthetic corticosteroid [dexamethasone (DEX)], we previously used the Federal Drug Administration-approved biodegradable polymers polycaprolactone (PCL), polylactic acid (PLA), polyglycolic acid (PGA), polyethylene glycol (PEG) and polylactide-co-glycolide (PLGA) (26, 27) to construct a nanoparticle (NP) pentablock (PB) copolymer (PGA–PCL–PEG–PCL–PGA) and encapsulate DEX (28).

In the current study, the effects of DEX delivered by our NP formulation were examined in vivo. Specifically, we used multiple

Significance

Glaucoma is the leading cause of irreversible blindness worldwide. The primary and only modifiable risk factor for the development of glaucoma is elevated intraocular pressure (IOP), and lowering IOP effectively slows glaucomatous disease progression. Unfortunately, the majority of available treatments do not target, or intentionally bypass, the diseased and stiffened glaucomatous outflow tissues responsible for IOP elevation. We recently established that conventional outflow tissue stiffness reflects tissue function. Therefore, detection of outflow tissue stiffness using noncontact, noninvasive optical coherence tomography, as we here demonstrate in an animal model of glaucoma, represents a valuable tool for assessing outflow tissue functional status. Such technology has the potential to monitor recently approved treatments targeting the outflow tissues, and to inform glaucoma surgery decisions.

Author contributions: G.L., J.M.S., S.F., P.G., C.-W.L., A.K.M., C.R.E., and W.D.S. designed research; G.L., C.L., V.A., K.W., I.N., K.C., and C.R.E. performed research; V.A., K.C., S.F., C.-W.L., A.K.M., C.R.E., and W.D.S. contributed new reagents/analytic tools; G.L., C.L., K.W., I.N., J.M.S., S.F., P.G., C.-W.L., A.K.M., C.R.E., and W.D.S. analyzed data; and G.L., C.L., K.W., J.M.S., K.C., C.R.E., and W.D.S. wrote the paper.

The authors declare no conflict of interest.

This article is a PNAS Direct Submission. J.S.S. is a guest editor invited by the Editorial Board.

[1]To whom correspondence may be addressed. Email: ross.ethier@bme.gatech.edu or dan.stamer@duke.edu.

This article contains supporting information online at www.pnas.org/lookup/suppl/doi:10.1073/pnas.1814889116/-/DCSupplemental.

Published online January 16, 2019.

approaches to study how DEX-loaded NPs (DEX-NPs) affected IOP, and corresponding changes in TM/SC biomechanics, fluid conductivity and morphology. We found that our DEX-loaded NPs elevated daytime IOPs to levels not observed previously in mouse models of steroid glaucoma. Moreover, spectral domain optical coherence tomography (SD-OCT) revealed that deformation of TM/SC due to changes in IOP was significantly attenuated in DEX-NP–treated mice. We then conducted inverse finite element modeling (FEM) to quantify increases in TM stiffness due to DEX-NPs. These findings suggest that SD-OCT–based noninvasive measurements of TM/SC stiffness can serve as a viable surrogate to assess the (dys)function of conventional outflow tissues in the eye, and establish a useful mouse model for better understanding the pathophysiology of steroid-induced and primary open-angle glaucoma.

Results

NP Delivery of DEX Causes Significant Daytime IOP Elevation Due to Increased Conventional Outflow Resistance. To overcome the short half-life of DEX in vivo, we previously formulated DEX-NPs and tested them in cell culture (28). Here we injected DEX-NPs into wild-type C57BL/6J mice, observing a sustained average daytime IOP elevation (Fig. 1*A*) using a combination of subconjunctival and periocular injections. Importantly, mice did not demonstrate body weight loss (*SI Appendix*, Fig. S1), a common drawback of other models of steroid-induced ocular hypertension based on systemic delivery of DEX (18, 29). IOP elevation was observed as early as 3 d after DEX-NP treatment. Further, IOP was titratable, with increased injection frequency inducing higher levels of IOP elevation (Fig. 1*B*; $P = 0.0004$): IOP elevations over baseline were 5.4 [95% confidence interval: 3.1, 7.7], 7.2 [4.8, 9.5], and 10.0 [8.7, 11.3] mmHg at two, four, and eight injections per month, respectively ($P < 0.001$ for all cases). No correlation was observed for control (CON)-NPs ($P = 0.3$), although a small increase in IOP of 1.8 [0.2, 3.4] mmHg ($P = 0.04$) was observed for eight injections per month. Unilateral injections were slightly less efficacious at two injections per month, but the difference relative to bilateral injections was not statistically significant (*SI Appendix*, Fig. S2).

Using liquid chromatography–mass spectrometry (LC/MS), DEX was detected intraocularly as early as 3 d after extraocular DEX-NP injection (Fig. 1*C*), with DEX levels increasing twofold at 1 wk compared with DEX levels at 3 d ($P = 0.03$). DEX levels were 1.5-fold higher with twice per week DEX-NP injections vs. once per week injections when examined at 7 d ($P = 0.03$). Using the iPerfusion system, specifically designed for measurements in mouse eyes, we found that outflow facility, a measure of fluid conductance through the outflow pathway tissues, was decreased by 23% in DEX-NP–treated mice ($P = 0.05$; Fig. 1*D*). Thus, IOP elevation in DEX-NP–treated mice was consistent with increased resistance (decreased outflow facility) in the conventional outflow tract.

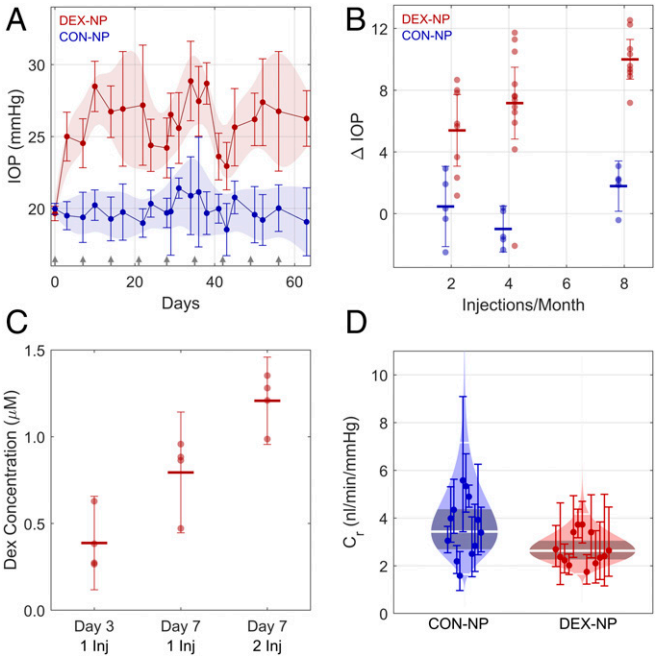

Fig. 1. Sustained delivery of DEX by custom NPs (DEX-NPs) induces ocular hypertension and decreased outflow facility in mice. (*A*) Sustained IOP elevation is observed in DEX-NP–treated eyes ($N = 7$ animals) versus CON-NP–treated eyes ($n = 5$ animals) from age- and gender-matched groups of mice injected subconjunctivally and/or periocularly with NPs once per week in both eyes (arrows indicate injection days for both groups). The data are shown as mean and 95% confidence interval over all animals. Shaded regions show 95% confidence bounds, smoothed with a cubic spline for visualization. (*B*) IOP elevation above baseline following different DEX-NP injection strategies at 3-wk time point. IOP elevation relative to baseline (ΔIOP) increased with increasing injection frequency ($P = 0.0005$). CON-NP injections had no detectible effect on IOP, irrespective of frequency. IOP elevations were 5.4 [95% confidence interval 3.1, 7.7], 7.2 [4.8, 9.5] and 10.0 [8.7, 11.3] mmHg at two, four, and eight injections per month, respectively. (*C*) DEX concentration in mouse eyes was measured at different time points using LC/MS/MS following injection (Inj) of DEX-NPs once or twice per week. Central lines show mean and error bars indicate 95% confidence intervals. For eyes receiving one injection, a higher DEX concentration was measured at day 7 than at day 3 ($P = 0.03$). At the 7-d time point, eyes receiving two injections had a higher DEX concentration than those receiving one injection ($P = 0.03$). The combined effects of time and number of injections yielded a significantly increased DEX concentration in the day 7, two-injection group compared with the Day 3, one-injection group ($P = 0.0004$). (*D*) Cello plots of outflow facility (45). All animals received one injection per week for 3 wk to 4 wk. Outflow facility in the CON-NP animals was 3.4 [2.2, 4.7] $nL{\cdot}min^{-1}{\cdot}mmHg^{-1}$ ($n = 12$) and was lower in DEX-NP–treated animals at 2.6 [1.5, 3.8] $nL{\cdot}min^{-1}{\cdot}mmHg^{-1}$ ($n = 13$), corresponding to a difference in outflow facility of −23% [−41%, 1%] that was borderline significant ($P = 0.05$). Shaded region indicates predicted log-normal distribution, with shaded band giving 95% confidence interval on the mean. Central white line shows mean value, with 2 SDs indicated by the outer white lines. Facility at 8 mmHg for each eye with 95% confidence intervals is shown by individual data points and error bars.

Pathological Changes Are Seen in the Conventional Outflow Pathway of DEX-NP–Treated Mouse Eyes. As in human corticosteroid-induced glaucoma, the iridocorneal angles of DEX-NP–treated mouse eyes (bilateral injections, once per week) were open, appearing grossly normal by light microscopy compared with CON-NP eyes (Fig. 2 *A* and *B*). However, upon closer inspection using immunofluorescence confocal microscopy, cellular and extracellular changes were evident. Specifically, both alpha-smooth muscle actin (α-SMA) and fibronectin (FN) levels were increased in the conventional outflow tract of DEX-NP–treated eyes (Fig. 2 *D* and *F*) compared with those in CON-NP–treated eyes (Fig. 2 *C* and *E*). These changes were confirmed by transmission electron microscopy (TEM), showing dramatic ultrastructural alterations in the juxtacanalicular region of the conventional outflow tract. In DEX-NP–treated eyes, there were decreased numbers of "open" intertrabecular spaces, and increased accumulation of amorphous extracellular matrix (ECM; Fig. 2 *G* and *H*). We also observed a more continuous basement membrane beneath the inner wall of SC in DEX-NP–treated eyes, compared with the typical discontinuous basement membrane in CON-NP–treated (Fig. 2 *G* and *H*).

SC Lumens in DEX-NP–Treated Eyes Were Resistant to IOP-Induced Collapse. Consistent with the gross "normal" appearance of conventional outflow tissues by standard histology, SD-OCT imaging of outflow tissues in living mice treated with DEX-NPs showed normal, open iridocorneal angle structures (Fig. 3). However, we found that, at the starting IOP of 10 mmHg, SC in DEX-NP–treated eyes was 29% larger than in CON-NP–treated eyes ($P = 0.04$; *SI Appendix*, Table S1), and, when challenged by

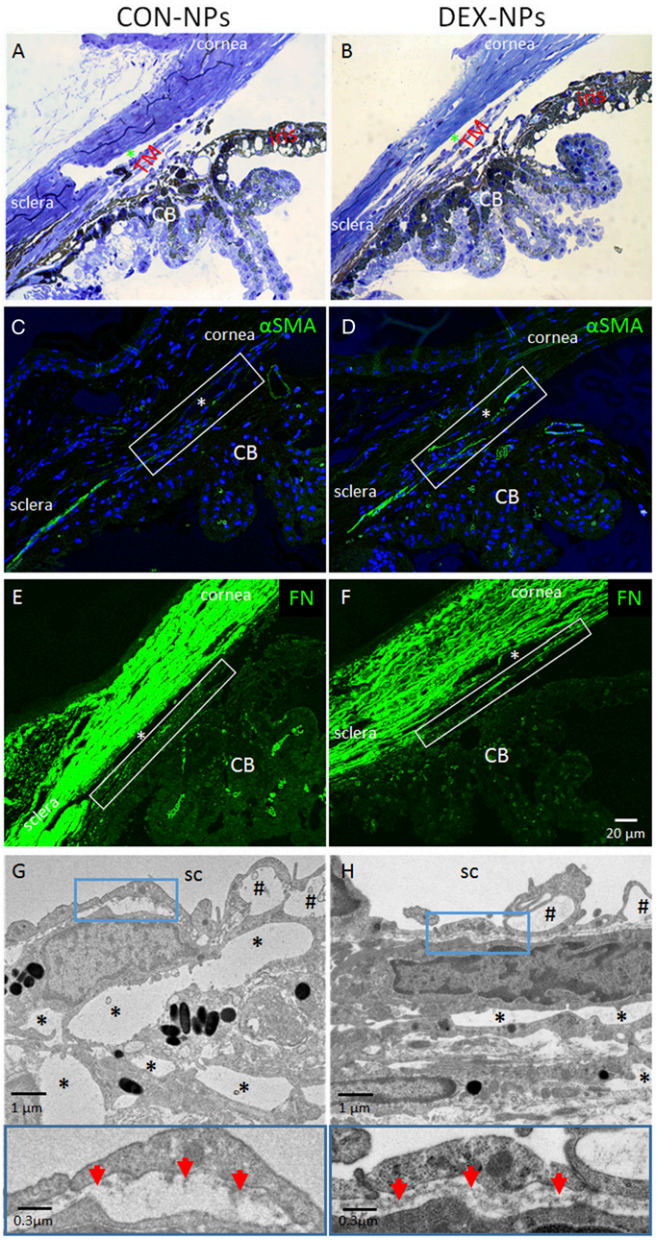

Fig. 2. Morphological changes in conventional outflow tissues of mouse eyes treated with DEX-NPs. Age- and gender-matched C57BL/6 mice were injected bilaterally once per week for 2 mo with either vehicle-loaded NPs (CON-NPs) or DEX-loaded NPs (DEX-NPs). (*A* and *B*) Iridocorneal angle tissue morphology of CON-NP– versus DEX-NP–injected mouse eyes, visualized by light microscopy after methylene blue staining, showed no gross difference between DEX-NP– and CON-NP–injected eyes. (*C*–*F*) Changes in α-SMA and FN levels in iridocorneal angle tissues of mouse eyes injected bilaterally with CON-NPs vs. DEX-NPs by immunofluorescence microscopy. Identical confocal settings were used for experimental and control groups. Conventional outflow tissues are outlined by white box, and nuclei are counterstained with DAPI. (*A*–*F*: scale bar, 20-μm.) (*G* and *H*) (*Top*) Ultrastructure of conventional outflow tissues in DEX-NP–treated eyes compared with CON-NP–treated eyes. Giant vacuoles in Schlemm's canal (SC) are indicated by hash marks. So-called "open spaces" in the juxtacanalicular region of the trabecular meshwork are indicated by asterisks. (*Bottom*) Boxed areas are enlarged, showing changes in basal lamina beneath SC endothelial cells. Red arrows indicate continuous basement membrane in DEX-NP–treated eyes compared with the discontinuous basal lamina seen in CON-NP–treated eyes (representative images from $n = 4$ animals); CB, ciliary body; *, SC lumen.

externally imposed sequential IOP elevations, SC in DEX-NP–treated eyes was more resistant to collapse than in control eyes (Fig. 3). This was quantified by segmentation of SC lumen area from all eyes, demonstrating significantly attenuated changes in SC dimensions in DEX-NP–treated eyes at all pressure steps tested (Fig. 3; $P = 0.007$ for 12 mmHg, and $P < 0.0002$ for higher pressures). The interobserver and intraobserver reproducibility for quantifying SC lumen area using the semiautomated SchlemmSeg software was very good, at 98.3% ± 8.1% and 99% ± 1.2%, respectively.

FEM of Conventional Outflow Tissue Responses to IOP Changes Shows Increased TM Stiffness in DEX-NP–Treated Eyes. We reasoned that the decreased propensity for SC to collapse after IOP elevation

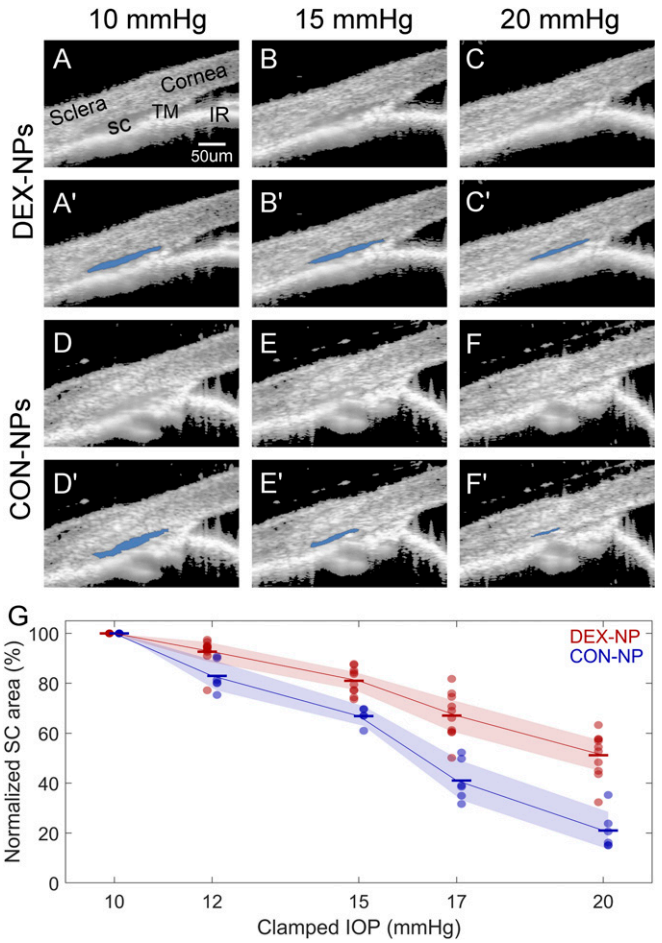

Fig. 3. Effects of DEX-NP treatment as visualized in living mice by OCT imaging. Living mouse eyes treated with DEX-NPs or CON-NPs were cannulated to control IOP and were subjected to sequentially increasing pressure steps (shown here are 10, 15, and 20 mmHg; all pressure steps are shown in *SI Appendix*, Fig. S5). (*A*–*F*) OCT imaging of conventional outflow tissues, viewed in cross-section, was conducted and images were averaged to reduce noise at each pressure step; (*A*′–*F*′) corresponding images show SC lumen segmentation by SchlemmSeg software with lumen overlaid in blue. Note the greater area of SC lumen in DEX-NP–treated eyes. IR, iris. (*G*) Quantitative comparison of SC lumen areas in both treatment groups (CON-NPs vs. DEX-NPs) at all clamped IOPs tested (10, 12, 15, 17, and 20 mmHg), confirming reduced tendency toward SC collapse in DEX-NP eyes. SC lumen area at each IOP level for each eye is normalized to the corresponding value at 10 mmHg. IOP is set (or "clamped") by adjusting the height of a fluid reservoir. Markers indicate individual eyes, and bars indicate mean values for each IOP. Shaded regions indicate 95% confidence intervals. Mice were injected subconjunctivally or periocularly once or twice per week for 2 mo ($n = 6$ CON-NP versus $n = 10$ DEX-NP).

in DEX eyes could be explained by TM stiffening, previously observed to correlate with aqueous outflow resistance in mouse and human eyes (24, 25). To estimate TM stiffness, we used an inverse FEM approach. A pseudo-2D FEM geometry (Fig. 4*B*) was created based on a typical OCT image (Fig. 4*A*), augmented by histology images (e.g., Fig. 2 *A* and *B*). The use of histology was important, since the OCT images lacked resolution in some of the finer anatomical details, notably the posterior extent of the iris–TM attachment, which had an appreciable influence on quantitative model predictions (*SI Appendix*, Fig. S3). Pressure loads were applied to the surfaces exposed to aqueous humor, including an estimated pressure within the lumen of SC, and the effects of the iris were accounted for by forces and moments at the virtual cut plane corresponding to the edge of the image. Simulations predicted significant strains within the iris root, and iris deformations that matched well with OCT images (Fig. 4*C*), enhancing confidence in the FEM results. By conducting simulations over a range of effective TM stiffnesses (20 kPa to 240 kPa), we found TM stiffness values that led to a best match (in the least-squares sense) between OCT and FEM results (Fig. 4*D*), suggesting that the TM in DEX-NP–treated eyes was approximately twice as stiff as in CON-NP–treated eyes (69 kPa vs. 29 kPa).

Discussion

We present a robust mouse model for corticosteroid-induced ocular hypertension using a custom NP-based delivery system. Delivery of DEX-loaded NPs (DEX-NPs) in mice led to elevated IOP, accompanied by reduced outflow facility and changes in conventional outflow tissues consistent with IOP elevation, including increased levels of extracellular matrix in the TM. Pressure elevations were observed as soon as 3 d after DEX-NP delivery; at least one other study (30) has seen a similarly rapid IOP elevation after DEX. Using in vivo OCT imaging, we also observed a reduced tendency toward SC collapse after IOP challenge in DEX-NP eyes. Extending an inverse FEM technique previously used in human eyes (24), high-resolution OCT images allowed us to estimate that DEX administration approximately doubled TM stiffness in living eyes. This approach has important clinical implications for noninvasive measurement of TM dysfunction in glaucoma patients with ocular hypertension, as discussed below.

The DEX-NP–induced ocular hypertension mouse model we generated has several advantages. First, our model showed minimal systemic adverse events. Compared with CON-NP–treated mice, we observed less than 1% body weight loss at 1 mo of treatment (*SI Appendix*, Fig. S1), in contrast to ∼30% body weight loss when using a systemic minipump approach to deliver DEX (22). Second, since the NPs were made from biodegradable and biocompatible materials, gross ocular morphology appeared normal after more than 2 mo of repeated NP injections (i.e., clear cornea, no cataracts, and a quiet ocular surface). A previous model used subconjunctival injections of triamcinolone acetonide in mice; however, IOPs were not significantly elevated in this model (31). Using a variation of this previous model to increase ocular DEX concentrations and reduce dosing frequency, a less

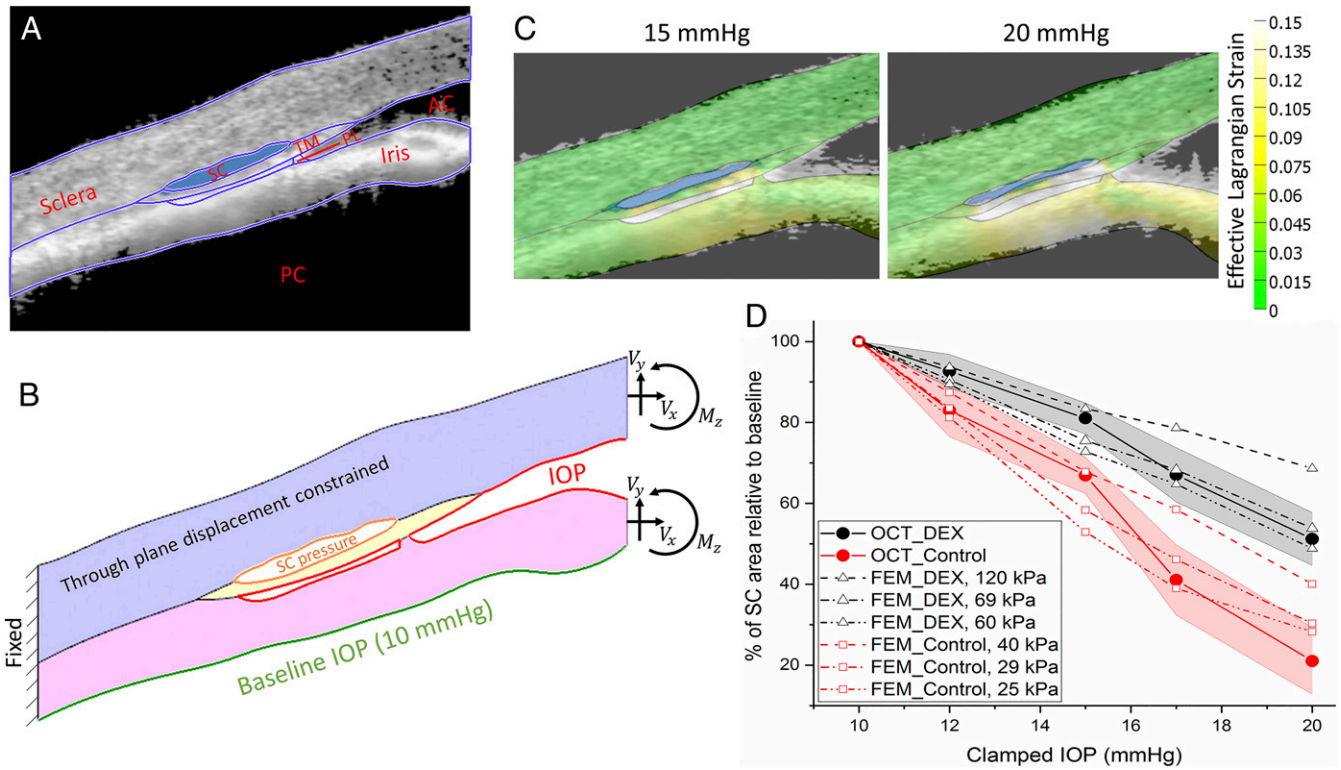

Fig. 4. Inverse FEM to estimate stiffness of mouse TM. (*A*) Representative OCT image of a DEX-NP–treated mouse overlain with tissue domains used to construct 2D finite element model. AC, anterior chamber; PC, posterior chamber; PL, pectinate ligament. (*B*) Resulting finite element model showing locations at which loads were applied, namely the lumen of SC, the anterior chamber, and the posterior iris, as well as the effective loads (V_x, V_y) and moment (M_z) acting on the virtual cut plane at the image boundary, arising from pressures acting on the iris and cornea. (*C*) Predicted tissue deformations and effective Lagrange strains (color) overlain on corresponding OCT images at 15 and 20 mmHg; note the reasonable agreement between iris position at both pressures. (*D*) Comparison between experimentally measured SC luminal area at different IOPs, and inverse FEM results, showing an approximately twofold difference in estimated effective TM stiffness (29 kPa in CON-NP–treated eyes vs. 69 kPa in DEX-NP–treated eyes). IOP is set (or clamped) by adjusting the height of a fluid reservoir. The shaded regions show 95% confidence intervals.

soluble DEX-21-acetate preparation was applied to mouse eyes by subconjuntival/periocular injection once per week for 4 wk. IOP was elevated as early as 1 wk without body weight loss (20). The local tolerability and/or biocompatibility of these crystals was not reported. Third, IOP levels in our model can be titrated by using various DEX-NP injection frequencies. For example, when using twice per month injections, we obtained daytime IOP elevations of ∼5 mmHg, while eight times per month injections elevated IOP by up to ∼10 mmHg. Importantly, DEX-treated eyes also displayed the major hallmarks of corticosteroid-induced ocular hypertension in humans, including decreased outflow facility, increased α-SMA–positive cells and FN in the outflow tract, and increased deposition of ECM in the juxtacanalicular region of the TM (ref. 22 and Figs. 1*D* and 2).

Surprisingly, we observed contralateral effects, i.e., ocular hypertension in the noninjected contralateral eye, when animals were injected unilaterally with DEX-NPs in early experiments (*SI Appendix*, Fig. S4). We cannot fully explain this finding, but we hypothesize that there may be venous or lymphatic communication between eyes. Interestingly, all three previous reports of ocular hypertension with local administration of DEX treated both eyes but did not comment on contralateral effects (20, 21, 32). Thus, we carried out injections bilaterally for all subsequent experiments.

Using our inverse FEM approach, we estimated the average TM stiffness in a living DEX-treated mouse eye to be 69 kPa, which is comparable to the stiffness of human glaucomatous TM we previously reported (79 kPa to 123 kPa) (24). It is important to note that the TM stiffness in DEX-treated mice that we report here is much higher than direct atomic force microscopy measurements of TM stiffness performed in this same model (DEX-treated: 2.38 ± 1.31 kPa; control: 1.99 ± 0.91 kPa). This is consistent with a previous report on human eyes in which TM stiffness measured by atomic force microscopy (AFM) was much less than, but closely correlated with, TM stiffness determined by an inverse FEM approach (24). Methodological differences likely explain these estimates. Specifically, in the inverse FEM approach, the TM was intact and was primarily stretched in the circumferential direction as IOP increased. In AFM studies, the TM was dissected from the eye and measured in a 10-μm-thick cryosection, primarily in compression. It is well known that the TM is under tension due to ciliary muscle tone (22) and that soft connective tissues are less stiff in compression than in tension (33). It is also important to note that the specific values of TM stiffness estimated by this approach were sensitive to fine anatomic details, particularly the location where the TM and iris merge posteriorly. Thus, although we report values for effective TM stiffnesses based on our best determination of the appropriate anatomy, a more robust outcome is the ratio of stiffnesses in DEX-NP– vs. CON-NP–treated eyes, which showed a consistent increase over a range of anatomic details.

The ability to estimate changes in TM stiffness using a completely noninvasive approach based on OCT imaging and FEM is an intriguing aspect of this work. Our approach can be categorized as a modified form of optical coherence elastography technology (34–38), which has been previously shown to be impactful for assessment of tissue elasticity in the anterior segment of the eye. In our approach, instead of utilizing external static or dynamic sources of displacements to mechanically load ocular tissue (e.g., air puff), we apply stress to the tissues by elevating IOP. We also exploit the unique anatomy of the outflow tract and monitor the collapse of SC, rather than tracking speckle patterns or employing other approaches to deduce local tissue strains. Thus, the mechanical properties that we infer should be interpreted as a spatially averaged value, ignoring local heterogeneities.

Several groups, including ours, have reported that TM stiffness positively correlates with increased outflow resistance in corticosteroid-induced ocular hypertensive mice (25), as well as in glaucomatous human donor eyes (24). The implication is that, since TM stiffness seems to be directly linked to conventional outflow function (25), detection of TM stiffness in living eyes may be clinically important, an observation that motivates further development of this technique. In another study, Pant et al. (39) estimated the stiffness of human TM in vivo using a FEM strategy similar to ours, finding a TM shear modulus of 1.93 kPa (approximately equivalent to an elastic modulus of 5.75 kPa) for the one sample they examined. Another study using a simplified beam-bending model based on in vivo changes in TM and SC deformation predicted a human TM stiffness (128 kPa) somewhat close to our estimates (40). However, in both of the above studies, pressure inside SC was not considered.

Recent advances in OCT imaging and image processing are important here: The high-resolution SD-OCT images of the mouse outflow tissues allowed us to determine reasonably clear boundaries of SC lumen, as reflected in the high interoperator and intraoperator repeatability of the SC segmentations. In view of the discussion above, further advances, specifically permitting more precise determination of the location where the iris and TM merge, would be beneficial and represent a future research target. Importantly, the larger human eye with its more open angle should be less prone to existing imaging limitations, suggesting that the combination of OCT imaging with inverse FEM is currently viable as a research tool to assess TM function in human eyes and could ultimately be developed into a clinically useful technique. Specifically, if TM tissue stiffness could be monitored in vivo using noncontact and noninvasive methods, the eye's outflow function could be accurately estimated, informing personalized treatment decisions. We envision this technology being applied to human eyes, where IOP is temporarily manipulated, e.g., after water drinking test or by external compression of the eye, while outflow tissues are imaged by OCT. Such a technique could serve as a more patient-friendly alternative to tonography (41) to assess TM function and status in glaucoma patients. It could also allow longitudinal tracking of TM stiffness in glaucoma patients to help monitor response to treatment and/or understand whether stiffening precedes ocular hypertension, or vice versa.

In future experiments involving mice, we are interested in examining the effects of aging and drug treatments on TM stiffness in vivo. It would be beneficial to know the range of stiffnesses that can be resolved in vivo using our OCT/FEM technology and compare stiffness determined in this way to outflow facility and to stiffnesses directly measured by AFM, as previously (25). For example, we would like to determine TM stiffnesses in rho kinase inhibitor-treated, untreated, and DEX-treated eyes, both in young and aged mice.

The present study had two primary limitations. Due to technical issues ultimately arising from the extreme precision required for accurate outflow facility measurements in the mouse, it was not feasible to measure outflow facility and to also estimate TM stiffness on a per-animal basis. However, in a previous study (25) conducted with the same mouse strain and using the same protocol executed by the same person (G.L.), we showed a strong correlation between outflow facility and TM stiffness as measured directly by AFM, which powerfully supports the link between these two parameters in the present study. Moreover, we compared IOP in DEX-NP mice from our previous study (25) vs. DEX-NP mice in the present study, and also compared IOP in CON-NP mice from the previous study vs. CON-NP mice in the present study, and found no statistical difference between the groups ($P > 0.05$ for both comparisons; unpaired t tests). This further supports the inference that TM stiffness, measured as we describe in the present manuscript, is related to outflow facility. A second limitation is that we only assessed one circumferential position in the inferior nasal region of each mouse eye. We chose this position due to reliable access in visualizing SC and because

we regularly found the SC lumen open, meaning that it likely coincided with an active flow region of the TM.

In conclusion, we have developed a biodegradable, biocompatible NP-based delivery system to generate a reliable and convenient DEX-induced mouse model of ocular hypertension. In this model, IOP levels can be controlled and maintained. Significantly, we detected and accurately estimated changes in conventional outflow tissue stiffness using OCT imaging coupled with FEM. Such advancements have potential clinical implications for early diagnosis, treatment, and prevention of vision loss in those with glaucoma.

Materials and Methods

Animals. Mice were handled in accordance with an approved protocol (A020-16-02) by Institutional Animal Care and Use Committee of Duke University and in compliance with the Association for Research in Vision and Ophthalmology (ARVO) Statement for the Use of Animals in Ophthalmic and Vision Research. C57BL/6 (C57) mice were purchased from the Jackson Laboratory, bred/housed in clear cages, and kept in housing rooms at 21 °C with a 12 h:12 h light:dark cycle. Mice were between 3 mo and 4 mo of age when experiments were initiated. Animal usage numbers and distribution are summarized in *SI Appendix*, Table S2.

DEX-NP or CON-NP Injections. DEX-NPs or CON-NPs were prepared as described (28). Briefly, PB copolymer of PGA–PCL–PEG–PCL–PGA) was synthesized by sequential ring-opening polymerization reaction. DEX-loaded PB copolymer NPs were prepared in the size range of ∼110 nm by oil-in-water single-emulsion solvent evaporation method. DEX-NPs or CON-NPs were diluted in PBS to a final NP concentration of 50 μg/μL, vortexed for 10 min, and then sonicated for 10 min. Mice were anesthetized with 100 mg/10 mg/kg of ketamine/xylazine. Then 20 μL of the NP suspension, containing 1 mg of NPs with ∼23 μg of DEX (or no DEX in control eyes), were slowly injected into either the superior or inferior subconjunctival or periocular spaces of a single eye or both eyes of mice using a 30-gauge needle with a Hamilton glass microsyringe (50-μL volume; Hamilton Company). Specifically, the initial two injections were subconjunctival, while subsequent injections were periocular to avoid complication of leaks following repeated subconjunctival injections. In experiments involving unilateral injections of DEX-NPs, a separate cohort of mice were used as controls, receiving unilateral injection of CON-NPs (*SI Appendix*, Fig. S2). After withdrawing the needle, Neomycin plus Polymyxin B Sulfate antibiotic ointment was applied to the eyes, and mice recovered on a warm pad.

Intraocular Pressure Measurements. The mice were anesthetized with ketamine (60 mg/kg) and xylazine (6 mg/kg). IOP was measured immediately upon cessation of movement (i.e., in light sleep) using rebound tonometry (TonoLab; Icare) between 1000 hours and 1300 hours (22, 42–44). Each recorded IOP was the average of six measurements, giving a total of 36 rebounds from the same eye per recorded IOP value. IOP measurements were conducted twice per week.

Outflow Facility Measurements. At designated time points, mice were killed using isoflurane, and eyes were carefully enucleated and mounted on a stabilization platform located in the center of a perfusion chamber using a small amount of cyanoacrylate glue (Loctite). The perfusion chamber was filled with prewarmed Dulbecco's PBS with added 5.5 mM D-glucose (DBG), submerging the eyes and regulating temperature at 35 °C. Two glass microneedles, back-filled with filtered DBG, were connected to the system. Using micromanipulators, one microneedle was inserted into each anterior chamber of paired eyes without contacting the irides. Both eyes were perfused at 9 mmHg for 30 min to allow acclimatization and stabilization, followed by perfusion at nine sequential pressure steps of 4.5, 6, 7.5, 9, 10.5, 12, 15, 18, and 21 mmHg. Poor-quality steps and subsequent pressure steps were eliminated. Stable flow rate (Q) and pressure (P) averaged over 4 min at each pressure step were used for data analysis (43–45). A nonlinear flow-pressure model [$Q = C_r(P/P_r)^{\beta}P$] that accounts for the pressure dependence of outflow facility in mice (β) was fit to the flow-pressure data using nonlinear regression, yielding the facility C_r evaluated at $P_r = 8$ mmHg, a pressure that approximates the physiological pressure drop across the conventional outflow pathway in living mice.

Measurements of DEX Concentration in Mouse Eyes. DEX-NPs (1.5 mg NPs/30 μL of PBS) containing ∼35 μg of DEX were injected bilaterally into the subconjunctival/periocular space in mice once or twice per week. Note that, for these experiments, we used a slightly greater volume of DEX-NPs than in other experiments, since DEX concentrations after our standard injections were below the detection limit of LC/MS/MS analysis. Three or seven days after DEX-NP injection, mice were killed using isoflurane, the eyes were enucleated, and the conjunctiva, Tenon's capsule, extraocular muscles, fatty tissues, and optic nerves were dissected free to isolate the globes, which were then rinsed in PBS. Eight naive C57BL/6 eyes were prepared using the same methods as controls. The whole eyes were frozen on dry ice and kept at −80 °C until DEX concentration measurements were performed. The eyes were weighed and transferred to bead mill tubes. A diluent consisting of 50:50 acetonitrile:water was added to tubes, and a bead mill was used to break up the tissue and extract DEX. Samples were then centrifuged before analysis. DEX levels in the supernatant were measured using LC/MS/MS, using a Bruker Elute UHPLC system coupled with a Bruker EVOQ Elite triple quadrupole mass spectrometer in multiple reaction monitoring mode. Method conditions for compound elution utilized a Waters XBridge BEH C18 column and water/acetonitrile mobile phase modified with formic acid. A calibration curve was prepared over the range of 1 ng/mL to 100 ng/mL by adding DEX to the samples prepared from C57 naïve eyes.

Histology, Immunohistochemistry, and TEM. Eight weeks after DEX-NP or CON-NP treatment (1 mg NP/20 μL of PBS, once per week injection bilaterally), animals were killed using isoflurane, and eyes were collected and immersion-fixed in 4% paraformaldehyde at 4 °C overnight. The eyes were then bisected, and the posterior segments and lenses were removed. The anterior segments were cut into four quadrants. For gross morphology studies of outflow tissues, each quadrant was embedded in Epon, and 0.5-μm semithin sections were cut, stained with 1% methylene blue, and examined by light microscopy (Axioplan2; Carl Zeiss MicroImaging). For immunostaining, each quadrant was embedded into LR-White, and 1-μm sections were cut and immunostained with antibodies that specifically recognized either α-SMA (1:100 dilution, rabbit polyclonal, ab5694; Abcam) or FN (1:50 dilution, mouse monoclonal; Santa Cruz). The secondary antibodies were peroxidase-conjugated AnffiniPure Goat Anti-Rabbit or mouse IgG H&L (Alexa Fluor 488; Jackson ImmunoResearch Laboratories) at 1:500 dilution. Images were captured using a Nikon Eclipse 90i confocal laser-scanning microscope (Melville). Images from experimental and control samples were collected at identical intensity and gain settings (z stacks of seven 0.5-μm optical sections for each image) (44). For electron microscopy studies, mouse anterior segments were embedded in Epon resin, and 65-nm sagittal sections were cut through iridocorneal tissues using an ultramicrotome (LEICA EM UC6, A-1170; Leica Mikrosysteme GmbH). Sections were stained with uranyl acetate/lead citrate and examined with a JEM-1400 electron microscope (JEOL USA).

Optical Coherence Tomographic Imaging. In vivo imaging utilized an Envisu R2200 high-resolution SD-OCT system (Bioptigen Inc.). We followed our previously established techniques to image iridocorneal angle structures in mice (22, 42, 43, 46). Briefly, after 2 mo of treatment with either CON-NPs or DEX-NPs, mice were anesthetized with ketamine (100 mg/kg)/xylazine (10 mg/kg) and maintained with ketamine (60 mg/kg) every 20 min by IP administration. While mice were secured in a custom-made platform, a single pulled glass microneedle filled with PBS was inserted into the anterior chamber of one eye. The microneedle was connected to both a manometric column to adjust IOP and a pressure transducer to continuously monitor IOP levels using PowerLab software. Our custom platform also provided a consistent angle between the imaging probe and the head of different mice. The OCT imaging probe was aimed at the nasal or temporal limbus, and the image was centered and focused on the SC lumen. While collecting images, mouse eyes were subjected to a series of IOP steps (10, 12, 15, 17, and 20 mmHg) by adjusting the height of the fluid reservoir. At each IOP step, a sequence of repeated OCT B scans (each with 1,000 A scans spanning 0.5 mm in lateral length) from spatially close positions was captured, registered, and averaged to create a high signal-to-noise-ratio image from the iridocorneal angle region of each animal. The duration of each pressure step was ∼1 min to 2 min. All imaging sessions were conducted by the same person (G.L.).

Segmentation of OCT Images. OCT B scans of iridocorneal angle tissues were registered and segmented following established methods (43) using SchlemmSeg software, which includes two modules: Schlemm I and Schlemm II. Briefly, OCT B scans were automatically registered using our custom Schlemm I software for SC segmentation. The Schlemm II software package was then used to differentiate SC from scleral vessels, which were automatically marked. If SC was seen connected to collector channels (CC), manual separation of SC from CC was required, and was based on the shape of SC and speckling in the images generated by blood cells or other

reflectors contained in blood vessels (22, 43, 47–50). The speckle variance OCT–angiography images were generated based on the speckling in SC and vessels as described in detail in a previous publication (43). SC was easily differentiated from other vessels, due to its size and location (*SI Appendix*, Fig. S5).

While the axial pixel pitch can be reliably calculated from theory, the pixel pitch converting the lateral pixel size to absolute distance in microns is an inaccurate estimate that depends on multiple factors, e.g., the distance of the probe from the image tissue and the refractive index of the tissues in the light path. For this reason, we report area ratios, i.e., SC lumen area relative to the SC lumen area at baseline IOP, instead of using and reporting absolute distance measurements given by our OCT system. Such ratios will not be affected by pixel pitch in an individual imaging session. For interested readers, the raw segmented data (in pixels) at each clamped IOP is provided in *SI Appendix*, Table S1.

Segmentation Reproducibility. To test the reproducibility of the SC segmentation process, we evaluated both interobserver and intraobserver reproducibility. The segmentation of SC was independently performed by two individuals. The first observer (G.L.) conducted the experiments and made initial measurements, then repeated the measurements 1 mo to 2 mo after the first examination to determine intraobserver reproducibility. When first analyzing the images, the first observer only knew the date of the experiment, not the treatment group. The treatment group was revealed after the lumen areas were calculated. The second observer (Caroline Wilson) was first given a training set of images to evaluate, then reviewed the images for the present study. This second observer was completely masked to assess the interobserver reproducibility.

FEM. Based on an OCT image of a typical DEX-treated eye at an IOP of 10 mmHg (baseline IOP; Fig. 4*A*), supplemented with histologic images of DEX-treated eyes (Fig. 2 *A* and *B*, and in multiple existing publications), we created a pseudo-2D FEM geometry in ICEM CFD (version 14.0; ANSYS, Inc.). The approach was similar to previous work in human tissue (24), where the model was formed by "extruding" the 2D cross-section for a distance of 10 μm from the averaged OCT scan. We refer to this model as the "SC lumen-focused model." In more detail, tissue components including the TM, sclera/cornea, and the uvea were carefully delineated from the chosen OCT scan (Fig. 4*B*). Four-noded tetrahedral elements with edge lengths from 5 μm to 13 μm were used for the mesh. After the meshed model was imported from ICEM CFD into PreView [part of the FEBio open-source suite (51)], tissues were treated as incompressible, isotropic, and nonlinearly hyperelastic (incompressible Mooney–Rivlin material model). Due to the absence of mouse-specific measurements of relevant stiffnesses, sclera/cornea stiffness was taken from human eyes as 2,700 kPa. Iridial stiffness was taken as 300 kPa, as estimated from a large-scale FEM informed by OCT images including the entire anterior segment (see below), and the TM was assigned a range of stiffnesses from 20 kPa to 240 kPa. For each TM stiffness value, we simulated the deformation of SC and the TM at each imposed IOP step, and determined the cross-sectional area of SC. The computed SC area was normalized by the SC area at an IOP of 10 mmHg, and this normalized value was compared with experimental measurements of SC area (Fig. 3), normalized in the same manner, i.e., against the SC cross-sectional area at 10 mmHg. The estimated TM stiffness was taken as the value that minimized the least-squares difference between the experimental and predicted normalized SC areas over the IOP range 10 mmHg to 20 mmHg.

The loading conditions were specified as follows. The imposed IOP was applied to all surfaces bounding the anterior chamber as well as the open space between the iris and TM (red curves in Fig. 4*B*). Here we reasoned that the pectinate ligament attachment between the TM and iris was focal, so that fluid pressure from the anterior chamber was transmitted into the open space between the iris and TM. The pressure applied to the posterior iris was taken as 10 mmHg; here we reasoned that the stepwise increasing IOP imposed during the testing protocol would lead to posterior iridial displacement and creation of a lens–iris diaphragm for IOPs above 10 mmHg, a supposition supported by OCT images of the entire anterior segment (*SI Appendix*, Fig. S3). Finally, the walls of SC had an estimated luminal pressure applied, as described below.

In addition to these pressure loads, we accounted for the effects of IOP on the portion of the iris and cornea falling outside the OCT image view by specifying effective forces and moments on a virtual cut plane at the edge of the SC lumen-focused model. To do so, we created a simplified, larger-scale finite element model of an entire anterior segment of a mouse eye using an OCT image at an IOP of 10 mmHg. The model included sclera, cornea, iris, and lens, as delineated from the OCT image using simple ellipsoids on a 2D plane. A 3D axisymmetric "wedge" model subtending 90° was than created by rotating the 2D outline by 90°, and an eight-noded hexahedral mesh with elements lengths of 10 μm to 60 μm was generated in ICEM CFD. We then simulated the effects of IOP elevations above 10 mmHg by applying a pressure load of IOP minus 10 mmHg to the surfaces bounding the anterior chamber. The sclera and cornea were modeled as a Mooney–Rivlin hyperelastic material with stiffness of 2,700 kPa, as in the SC-focused model. The lens was modeled as a rigid body, since it is much stiffer than other tissues. We treated the iris as a Mooney–Rivlin hyperelastic material and tested several iris stiffnesses to match the predicted and observed iris deformations as IOP was increased above 10 mmHg (*SI Appendix*, Fig. S3). An iris stiffness of 300 kPa showed reasonable agreement (yellow lines in *SI Appendix*, Fig. S3). We then extracted stresses at nodes on a line coinciding approximately with the edge of the SC lumen-focused model (green dashed line in *SI Appendix*, Fig. S3). Shear and normal tractions at the cut edge of the iris and sclera were calculated by suitably transforming the stress tensors and integrating the relevant components along the cut line. The effective moment was calculated in an analogous fashion. The resulting tractions and moments were applied to the virtual cut planes of the iris and cornea as shown in Fig. 4*B*. We acknowledge that this is a simplification, and a fuller treatment would necessitate a more complex model that acknowledged fluid–iris interactions in the posterior and anterior chambers. However, in view of the good agreement between predicted and measured iris deformations in the SC-lumen focused model (Fig. 4*C*), we feel that the above approach was reasonable.

Since no direct measurements of SC luminal pressure have been conducted in mouse eyes due to the inherent technical challenges of such a measurement, we were forced to estimate the pressure within the lumen of SC, as follows. The conventional outflow pathway was modeled as two series resistors (*SI Appendix*, Fig. S3), representing the TM/inner wall of SC ($R_{TM/SC}$) and the distal vessels (R_{dist}). The pressure in SC lumen, P_{SC}, can then be written as

$$P_{SC} = \frac{R_{dist}(\mathrm{IOP}) + R_{TM/SC}(\mathrm{EVP})}{R_{TM/SC} + R_{dist}}, \quad [1]$$

where EVP is episcleral venous pressure. Dividing through by R_{dist} and introducing $R^* = R_{TM/SC}/(R_{TM/SC} + R_{dist})$ yields

$$P_{SC} = \left(1 - R^*\right)\mathrm{IOP} + R^*(\mathrm{EVP}). \quad [2]$$

For control eyes, we took $R^*_{CON} = 0.6$, as it has been reported in humans that 49 to 71% of the resistance to aqueous humor outflow is localized to the TM, depending on the level of IOP (52, 53). For DEX-treated eyes, assuming that R_{dist} is unaffected by DEX, we can write

$$R^*_{DEX} = 1 - \frac{C_{DEX}}{C_{CON}}\left(1 - R^*_{CON}\right). \quad [3]$$

The measured values of C_{DEX} and C_{CON} can then be used to calculate R^*_{DEX}. Alternatively, if it is assumed that the difference between aqueous humor inflow and pressure-independent outflow is not affected by DEX treatment, i.e., that the major effect of DEX is simply to alter conventional outflow facility (54–57), then the C terms can be replaced by

$$\frac{C_{DEX}}{C_{CON}} = \frac{\mathrm{IOP}_{CON} - \mathrm{EVP}}{\mathrm{IOP}_{DEX} - \mathrm{EVP}}. \quad [4]$$

Measured values of IOP and C were then used for each case to define P_{SC} with Eqs. **2** and **3** (*SI Appendix*, Table S3), assuming that EVP was 5.4 mmHg (58) and was unaffected by DEX. Interestingly, the ratio of directly measured facilities was very close to that predicted by Eq. **4**, suggesting that DEX did indeed primarily affect conventional outflow facility in mice.

Statistical Analysis. For all analyses, where data existed for both eyes from a single mouse, the average from the contralateral eyes was used. With the exception of outflow facility measurements, the Anderson–Darling test was used for all analyses to evaluate normality before selecting statistical tests. In these cases, the assumption of normality was not rejected. For outflow facility measurements, we used well-established statistics (45) based upon a large sample size, establishing that the underlying distribution of outflow facility in mice is log-normally distributed.

For the longitudinal IOP analysis (Fig. 1*A*), the Anderson–Darling test did not reject normality for all except 2/21 DEX-NP and 1/21 CON-NP timepoints. A two-way t test was thus used to compare the DEX-NP data to the CON-NP data for each time point.

To evaluate whether there was a correlation between IOP elevation and injection frequency (Fig. 1*B*), Spearman's rank correlation coefficient was applied, as the correlation is not necessarily expected to be linear. For each time point, the Anderson–Darling test did not reject normality, and hence a one-way *t* test was used to evaluate whether the IOP elevation was significantly different from zero.

For DEX concentration analysis (Fig. 1*C*), the Anderson–Darling test did not reject normality for any of the three groups, nor did Levene's quadratic test reject equal variances between cases. Hence, a one-way ANOVA was used to compare the effects of time and number of injections. A Tukey–Kramer post hoc test was used to evaluate significance for pairwise comparisons between groups.

For analysis of outflow facility (Fig. 1*D*), all data were analyzed as log-normally distributed parameters (45). A weighted unpaired (two-way) *t* test (45) was applied to the log-transformed facilities. Final average values of facility thus represent the geometric mean and are provided with 95% confidence intervals. Where both eyes were used, the uncertainties (in the log domain) were added in quadrature.

Data in box and whisker plots show median, 25th percentile, and 75th percentile (boxes), as well as minimum and maximum values (whiskers). Data in other plot formats are presented in the form of mean (95% confidence interval) throughout. A value of $P \leq 0.05$ was considered statistically significant.

ACKNOWLEDGMENTS. We thank Ying Hao (Duke Eye Center Core Facility), who prepared histology sections and helped with TEM. Dr. Vivek Agrahari helped with the preparation and characterization of the NPs. We also acknowledge Lori Moore (Aerie Pharmaceuticals, Inc.), who helped with delivery of mouse eye samples, and Caroline Wilson, who helped with OCT imaging analysis. We acknowledge funding support from the BrightFocus Foundation, Research to Prevent Blindness Foundation, the National Eye Institute (Grants EY005722 and EY019696), and the Georgia Research Alliance.

1. Ciulla TA, Walker JD, Fong DS, Criswell MH (2004) Corticosteroids in posterior segment disease: An update on new delivery systems and new indications. *Curr Opin Ophthalmol* 15:211–220.
2. Lautredou CC, et al. (2018) Repeat intravitreal dexamethasone implant for refractory cystoid macular edema in syphilitic uveitis. *Case Rep Ophthalmol Med* 2018:7419823.
3. Al-Khersan H, Hariprasad SM, Chhablani J; Dex Implant Study Group (2017) Early response to intravitreal dexamethasone implant therapy in diabetic macular edema may predict visual outcome. *Am J Ophthalmol* 184:121–128.
4. Miller K, Fortun JA (2018) Diabetic macular edema: Current understanding, pharmacologic treatment options, and developing therapies. *Asia Pac J Ophthalmol (Phila)* 7:28–35.
5. Narayanan R, Kuppermann BD (2017) Corticosteroids and anti-complement therapy in retinal diseases. *Handb Exp Pharmacol* 242:309–320.
6. Schwartz SG, Scott IU, Stewart MW, Flynn HW, Jr (2016) Update on corticosteroids for diabetic macular edema. *Clin Ophthalmol* 10:1723–1730.
7. Haller JA, et al.; Ozurdex GENEVA Study Group (2011) Dexamethasone intravitreal implant in patients with macular edema related to branch or central retinal vein occlusion twelve-month study results. *Ophthalmology* 118:2453–2460.
8. Coassin M, et al. (2016) Bromfenac ophthalmic solution 0.09% as an adjunctive therapy to topical steroids after cataract surgery in pseudoexfoliation syndrome. *J Cataract Refract Surg* 42:1119–1125.
9. Dibas A, Yorio T (2016) Glucocorticoid therapy and ocular hypertension. *Eur J Pharmacol* 787:57–71.
10. Bhattacherjee P, Paterson CA, Spellman JM, Graff G, Yanni JM (1999) Pharmacological validation of a feline model of steroid-induced ocular hypertension. *Arch Ophthalmol* 117:361–364.
11. Fingert JH, et al. (2001) Evaluation of the myocilin (MYOC) glaucoma gene in monkey and human steroid-induced ocular hypertension. *Invest Ophthalmol Vis Sci* 42: 145–152.
12. Gerometta R, et al. (2004) Steroid-induced ocular hypertension in normal cattle. *Arch Ophthalmol* 122:1492–1497.
13. Gerometta R, Podos SM, Danias J, Candia OA (2009) Steroid-induced ocular hypertension in normal sheep. *Invest Ophthalmol Vis Sci* 50:669–673.
14. Knepper PA, Breen M, Weinstein HG, Blacik JL (1978) Intraocular pressure and glycosaminoglycan distribution in the rabbit eye: Effect of age and dexamethasone. *Exp Eye Res* 27:567–575.
15. Lorenzetti OJ (1970) Effects of corticosteroids on ocular dynamics in rabbits. *J Pharmacol Exp Ther* 175:763–772.
16. Sawaguchi K, Nakamura Y, Nakamura Y, Sakai H, Sawaguchi S (2005) Myocilin gene expression in the trabecular meshwork of rats in a steroid-induced ocular hypertension model. *Ophthalmic Res* 37:235–242.
17. Zhan GL, Miranda OC, Bito LZ (1992) Steroid glaucoma: Corticosteroid-induced ocular hypertension in cats. *Exp Eye Res* 54:211–218.
18. Whitlock NA, McKnight B, Corcoran KN, Rodriguez LA, Rice DS (2010) Increased intraocular pressure in mice treated with dexamethasone. *Invest Ophthalmol Vis Sci* 51: 6496–6503.
19. SooHoo JR, Seibold LK, Laing AE, Kahook MY (2012) Bleb morphology and histology in a rabbit model of glaucoma filtration surgery using Ozurdex® or mitomycin-C. *Mol Vis* 18:714–719.
20. Patel GC, et al. (2017) Dexamethasone-induced ocular hypertension in mice: Effects of myocilin and route of administration. *Am J Pathol* 187:713–723.
21. Zode GS, et al. (2014) Ocular-specific ER stress reduction rescues glaucoma in murine glucocorticoid-induced glaucoma. *J Clin Invest* 124:1956–1965.
22. Li G, et al. (2014) Pilocarpine-induced dilation of Schlemm's canal and prevention of lumen collapse at elevated intraocular pressures in living mice visualized by OCT. *Invest Ophthalmol Vis Sci* 55:3737–3746.
23. Last JA, et al. (2011) Elastic modulus determination of normal and glaucomatous human trabecular meshwork. *Invest Ophthalmol Vis Sci* 52:2147–2152.
24. Wang K, et al. (2017) Estimating human trabecular meshwork stiffness by numerical modeling and advanced OCT imaging. *Invest Ophthalmol Vis Sci* 58:4809–4817.
25. Wang K, et al. (2018) The relationship between outflow resistance and trabecular meshwork stiffness in mice. *Sci Rep* 8:5848.
26. Yang X, et al. (2016) Nanoparticle-based topical ophthalmic gel formulation for sustained release of hydrocortisone butyrate. *AAPS PharmSciTech* 17:294–306.
27. Boddu SH, et al. (2010) Novel nanoparticulate gel formulations of steroids for the treatment of macular edema. *J Ocul Pharmacol Ther* 26:37–48.
28. Agrahari V, et al. (2017) Pentablock copolymer dexamethasone nanoformulations elevate MYOC: In vitro liberation, activity and safety in human trabecular meshwork cells. *Nanomedicine (Lond)* 12:1911–1926.
29. Overby DR, et al. (2014) Ultrastructural changes associated with dexamethasone-induced ocular hypertension in mice. *Invest Ophthalmol Vis Sci* 55:4922–4933.
30. Borrás T, Buie LK, Spiga MG (2016) Inducible scAAV2.GRE.MMP1 lowers IOP long-term in a large animal model for steroid-induced glaucoma gene therapy. *Gene Ther* 23: 438–449.
31. Kumar S, Shah S, Deutsch ER, Tang HM, Danias J (2013) Triamcinolone acetonide decreases outflow facility in C57BL/6 mouse eyes. *Invest Ophthalmol Vis Sci* 54: 1280–1287.
32. Patel GC, Liu Y, Millar JC, Clark AF (2018) Glucocorticoid receptor GRβ regulates glucocorticoid-induced ocular hypertension in mice. *Sci Rep* 8:862.
33. Ethier CR, Simmons CA (2007) *Introductory Biomechanics From Cells to Organisms* (Cambridge Univ Press, Cambridge, UK).
34. Kennedy BF, Wijesinghe P, Sampson DD (2017) The emergence of optical elastography in biomedicine. *Nat Photonics* 11:215–221.
35. Schmitt J (1998) OCT elastography: Imaging microscopic deformation and strain of tissue. *Opt Express* 3:199–211.
36. Kirby MA, et al. (2017) Optical coherence elastography in ophthalmology. *J Biomed Opt* 22:1–28.
37. Larin KV, Sampson DD (2017) Optical coherence elastography–OCT at work in tissue biomechanics [invited]. *Biomed Opt Express* 8:1172–1202.
38. Singh M, et al. (2017) Applanation optical coherence elastography: Noncontact measurement of intraocular pressure, corneal biomechanical properties, and corneal geometry with a single instrument. *J Biomed Opt* 22:20502.
39. Pant AD, Kagemann L, Schuman JS, Sigal IA, Amini R (2017) An imaged-based inverse finite element method to determine *in-vivo* mechanical properties of the human trabecular meshwork. *J Model Ophthalmol* 1:100–111.
40. Johnson M, Schuman JS, Kagemann L (2015) Trabecular meshwork stiffness in the living human eye. *Invest Ophthalmol Visual Sci* 56:3541.
41. Kazemi A, et al. (2017) Comparison of aqueous outflow facility measurement by pneumatonography and digital Schiøtz tonography. *Invest Ophthalmol Vis Sci* 58: 204–210.
42. Li G, et al. (2014) Disease progression in iridocorneal angle tissues of BMP2-induced ocular hypertensive mice with optical coherence tomography. *Mol Vis* 20:1695–1709.
43. Li G, et al. (2016) Visualization of conventional outflow tissue responses to netarsudil in living mouse eyes. *Eur J Pharmacol* 787:20–31.
44. Li G, et al. (2018) Trabodenoson, an adenosine mimetic with A1 receptor selectivity lowers intraocular pressure by increasing conventional outflow facility in mice. *Invest Ophthalmol Vis Sci* 59:383–392.
45. Sherwood JM, Reina-Torres E, Bertrand JA, Rowe B, Overby DR (2016) Measurement of outflow facility using iPerfusion. *PLoS One* 11:e0150694.
46. Boussommier-Calleja A, et al. (2015) Physical factors affecting outflow facility measurements in mice. *Invest Ophthalmol Vis Sci* 56:8331–8339.
47. Hendargo HC, et al. (2013) Automated non-rigid registration and mosaicing for robust imaging of distinct retinal capillary beds using speckle variance optical coherence tomography. *Biomed Opt Express* 4:803–821.
48. Huang Q, Zheng Y, Lu M, Wang T, Chen S (2009) A new adaptive interpolation algorithm for 3D ultrasound imaging with speckle reduction and edge preservation. *Comput Med Imaging Graph* 33:100–110.
49. Mariampillai A, et al. (2008) Speckle variance detection of microvasculature using swept-source optical coherence tomography. *Opt Lett* 33:1530–1532.
50. Poole KM, McCormack DR, Patil CA, Duvall CL, Skala MC (2014) Quantifying the vascular response to ischemia with speckle variance optical coherence tomography. *Biomed Opt Express* 5:4118–4130.
51. Maas SA, Ellis BJ, Ateshian GA, Weiss JA (2012) FEBio: Finite elements for biomechanics. *J Biomech Eng* 134:011005.
52. Rosenquist R, Epstein D, Melamed S, Johnson M, Grant WM (1989) Outflow resistance of enucleated human eyes at two different perfusion pressures and different extents of trabeculotomy. *Curr Eye Res* 8:1233–1240.

53. Overby DR, Stamer WD, Johnson M (2009) The changing paradigm of outflow resistance generation: Towards synergistic models of the JCT and inner wall endothelium. *Exp Eye Res* 88:656–670.
54. Armaly MF (1963) Effect of corticosteroids on intraocular pressure and fluid dynamics. I. The effect of dexamethasone in the normal eye. *Arch Ophthalmol* 70:482–491.
55. Kupfer C, Ross K (1971) Studies of aqueous humor dynamics in man. I. Measurements in young normal subjects. *Invest Ophthalmol* 10:518–522.
56. Nicholas JP (1964) Topical corticosteroids and aqueous humor dynamics. *Arch Ophthalmol* 72:189–197.
57. Anselmi P, Bron AJ, Maurice DM (1968) Action of drugs on the aqueous flow in man measured by fluorophotometry. *Exp Eye Res* 7:487–496.
58. Millar JC, Clark AF, Pang IH (2011) Assessment of aqueous humor dynamics in the mouse by a novel method of constant-flow infusion. *Invest Ophthalmol Vis Sci* 52: 685–694.